CHEMISTRY

Unlocking iron metal as a cathode for sustainable Li-ion batteries by an anion solid solution

Mingliang Yu[1], Jing Wang[2], Ming Lei[3], Min Soo Jung[1,4], Zengqing Zhuo[5], Yufei Yang[6], Xueli Zheng[6,7], Sean Sandstrom[1], Chunsheng Wang[8], Wanli Yang[5]*, De-en Jiang[3]*, Tongchao Liu[2]*, Xiulei Ji[1]*

Traditional cathode chemistry of Li-ion batteries relies on the transport of Li-ions within the solid structures, with the transition metal ions and anions acting as the static components. Here, we demonstrate that a solid solution of F^- and PO_4^{3-} facilitates the reversible conversion of a fine mixture of iron powder, LiF, and Li_3PO_4 into iron salts. Notably, in its fully lithiated state, we use commercial iron metal powder in this cathode, departing from electrodes that begin with iron salts, such as FeF_3. Our results show that Fe-cations and anions of F^- and PO_4^{3-} act as charge carriers in addition to Li-ions during the conversion from iron metal to a solid solution of iron salts. This composite electrode delivers a reversible capacity of up to 368 mAh/g and a specific energy of 940 Wh/kg. Our study underscores the potential of amorphous composites comprising lithium salts as high-energy battery electrodes.

INTRODUCTION

A tremendous transition takes place to replace fossil fuels with Li-ion batteries (LIBs) to power transportation (*1*). However, the LIBs used in electric vehicles are unsustainable because they use cathodes of Ni-rich layered metal oxides, i.e., $LiMO_2$, such as $LiNi_xCo_yAl_zO_2$ (NCA) and $LiNi_xMn_yCo_zO_2$ (NMC), that face the foreseeable shortage of cobalt and nickel in the near future (*2*–*6*). The cathode accounts for over 50% of the cell cost of LIBs (*7*); nevertheless, they have reached the ceiling of the safety-allowed energy density (*8*, *9*). Therefore, it is pivotal to invent a sustainable cathode chemistry that offers high energy density (*10*). In a typical LIB cell, Li-ions serve as a charge carrier for the half-cell reactions at electrodes and the overall reaction of the full cell. At the half-cell level, Li-ions are incorporated or expelled by the electrodes for charge neutrality, and at the full-cell level, Li-ions commute between the electrodes to achieve the balance of charges and mass for the overall reaction. Nevertheless, progress in dual-ion batteries (DIBs) has demonstrated that anions can charge-neutralize the operating electrodes (*11*, *12*). In DIBs, during battery charge, the cathode and anode glean anions and cations, respectively, from the electrolyte. Unfortunately, the fact that all ions are initially stored in the electrolyte renders the energy density of DIBs low because of the limitation of the electrolyte volume and concentration (*13*–*15*). However, the most concentrated liquid electrolyte still has a lower Li concentration than that in solid lithium salts. To promote energy density, such solid-state salts can be finely mixed with the anion-hosting active mass of the cathode. We refer to such an electrode as the lithium-salt-composite (LSC) electrode, where the redox-active mass serves as the electron source and an anion host, and the lithium salt acts as the source of ion charge carriers. In an LSC cathode, during charging, the lithium salt dissociates Li-ions to migrate to the anode via the liquid electrolyte, where the counter anions transport locally to form ionic bonds with the cathode host.

In the LSC cathodes, metals represent attractive electron sources due to their large theoretical capacity values, low cost, and high density. Several examples of metal-based LSC cathodes have been reported. Dahn and colleagues reported the chargeability of M/Li_2O, M/Li_2S, and M/LiF composites, where M is a transition metal (*16*, *17*). To date, LiF has been the default choice of lithium salt for LSC electrodes that have Ti (*18*), Fe (*19*–*22*), Cu (*23*), Co (*24*), and metal monoxides (*25*) as the electron source. The conversion of these metals to their metal fluorides is considered the "absorption" of fluoride ions within the domains of nanocomposites (*26*) or thin films formed by pulsed laser deposition (*27*), where both the electron source and LiF are nanosized and intimately mixed. Notably, the electrochemical properties of such electrodes are widely attributed to the transport of Li-ions and their storage through a conversion reaction at the grain boundaries, where the anion transport receives meager attention (*28*). The challenges of LiF-based LSC electrodes are that they exhibit a large potential hysteresis and a low discharge potential (versus Li^+/Li, and hereafter). To address the challenges, strategies usually focused on tuning the metal side, such as doping iron with another metal, e.g., Ni or Cu, to promote the "splitting" of LiF (*29*, *30*). Of note, the choice of fluoride in such electrodes is rarely challenged. Most research has been devoted to the conversion of metal compounds with a single anion, suffering a large charge-discharge hysteresis (*31*–*34*). Recently, Wang and colleagues reported an LSC cathode that consists of micrometer-sized graphite and solid LiCl and LiBr. This electrode benefits from the slight solubility of the halide salts in the electrolyte, which confers the transport of halides and their intercalation into graphite galleries (*35*). Despite the tremendous progress made, basic questions have yet to be addressed: Can one use submicrometer iron particles in the LSC cathode, and can the anion environment be designed to activate the iron active mass?

Here, we report the formation of an LSC electrode comprising iron and a solid solution of amorphous lithium fluoride and lithium

[1]Department of Chemistry, Oregon State University, Corvallis, OR 97331, USA. [2]Chemical Sciences and Engineering Division, Argonne National Laboratory, Lemont, IL 60439, USA. [3]Department of Chemical and Biomolecular Engineering, Vanderbilt University, Nashville, TN 37235, USA. [4]School of Chemical and Biological Engineering, Seoul National University, Seoul 08826, Republic of Korea. [5]Advanced Light Source, Lawrence Berkeley National Laboratory, Berkeley, CA 94720, USA. [6]Materials Science and Engineering, Stanford University, Stanford, CA 94305, USA. [7]Applied Energy Division, SLAC National Accelerator Laboratory, Menlo Park, CA 94025, USA. [8]University of Maryland, College Park, MD 20742, USA.
*Corresponding author. Email: wlyang@lbl.gov (W.Y.); de-en.jiang@vanderbilt.edu (D.J.); liut@anl.gov (T.L.); david.ji@oregonstate.edu (X.J.)

phosphate. Compared with the composites consisting of iron with a single lithium salt, the anion solid solution exhibits much improved performance, comparable to the Ni-rich cathode materials. The ternary iron-based composite delivers a capacity of up to 368 mAh/g and a specific energy (versus Li) of 940 Wh/kg with stable cycling.

RESULTS

Screening lithium salts for the iron-based LSC

We first screened Fe/Li_xA LSC cathodes with different anions (A^{x-}) of high charge/mass ratios, including F^-, PO_4^{3-}, CO_3^{2-}, and SO_4^{2-}, by comparing their galvanostatic charge-discharge (GCD) performance. These composites were processed by ball milling a mixture comprising bulk iron powder, individual lithium salts, and graphite (20 wt%) under an Ar atmosphere with Fe/Li_xA molar ratios corresponding to the three-electron transfer of iron to form ferric Fe_xA_3. Figure S1 depicts the morphology of the composites after ball milling. It is well known that ball milling exfoliates graphite into graphene sheets (*36*), thus providing an electronic conduit for lithium salts in the LSC electrodes (*37*). Fe/LiF exhibits a reversible capacity of 242 mAh/g with an average discharge potential of 2.4 V, where 50% of its capacity originates from the lower quasi-plateau below 2 V, which is similar to the previous reports (Fig. 1A) (*19*, *20*, *38*). Notably, Fe/Li_3PO_4 exhibits a reversible discharge capacity at 181 mAh/g with 30% of its capacity below 2 V (Fig. 1B). Of note, both Fe/LiF and Fe/Li_3PO_4 composite electrodes display a large potential hysteresis in the first cycle (fig. S2), where the first charging potential is substantially higher than the potentials of later charging processes. Notably, the hysteresis shrinks along cycling, where the initial cycles serve as a conditioning process. Figure S3 illustrates a decline in the overpotentials for both charge and discharge profiles, with an enhancement in energy efficiency. The conditioning process with repeated cycles of ion relocations facilitates structural alterations in the electrode materials, resulting in expedited ion diffusion. However, both Fe/Li_2CO_3 and Fe/Li_2SO_4 presented poor reversibility and exhibited subpar capacity values compared to Fe/LiF and Fe/Li_3PO_4 (fig. S4).

Anion solid solution mixed with iron

Considering that Fe/LiF favors a high utilization of iron and Fe/Li_3PO_4 confers a high discharge potential, and that anion mobility may play a role in the operation of LSC electrodes, we postulate that the presence of a solid solution of PO_4^{3-} and F^- in the LSC electrode may integrate the benefits of both Fe/LiF and Fe/Li_3PO_4 systems. Cation solid solutions are widely used to improve the performance of cathode materials of LIBs such as in layered metal oxide cathodes (*2*), and anionic solid solutions are well known particularly in the fluoride phosphates (*39*, *40*). In the conventional LIB cathodes, anions such as oxide, phosphate, or two anions in a solid solution are the building blocks of the ordered structural frameworks, which are deemed immobile in battery cycling. However, in an amorphous LSC cathode, the transport of anions may be necessary for the electrode charging, so we investigated whether anions play a more active role with a solid solution of PO_4^{3-} and F^- in an amorphous structure.

We first compared the performance of the ternary composite electrodes formed by ball milling the pertinent salts and iron with different molar ratios of Li_3PO_4 and LiF: 1:2, 1:1, and 2:1, where the

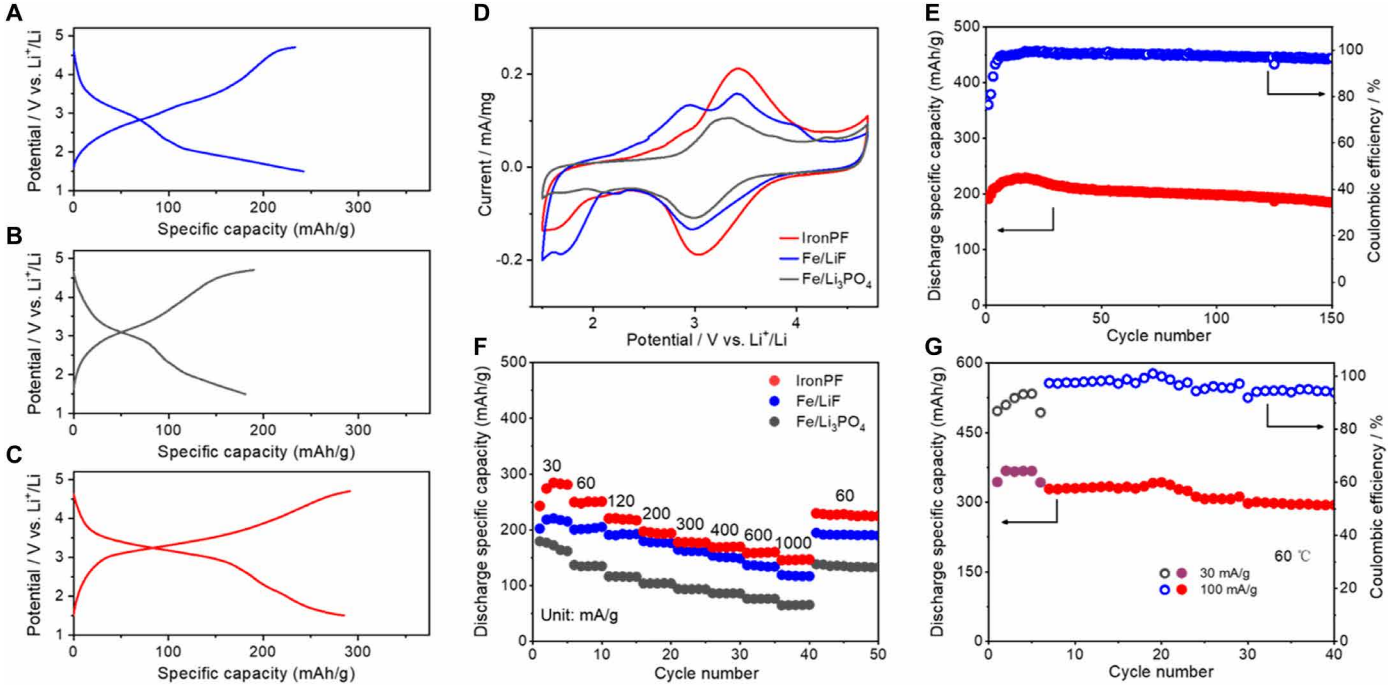

Fig. 1. Electrochemical performance of the LSC cathodes. GCD potential profiles at 30 mA/g of the LSC electrodes of (**A**) Fe/LiF, (**B**) Fe/Li_3PO_4, and (**C**) IronPF. All GCD cycles are from the 11th cycle, where the composite electrodes have undergone 10 conditioning cycles at 100 mA/g. The initial cycling profiles are shown in fig. S2. (**D**) CV curves of Fe/LiF, Fe/Li_3PO_4, and IronPF electrodes at 0.2 mV/s with current normalized on the basis of the mass of the active materials. (**E**) Cycling performance of IronPF at 100 mA/g. (**F**) Rate capability of Fe/LiF, Fe/Li_3PO_4, and IronPF electrodes. (**G**) Cycling performance of IronPF at 60°C at the current rate of 30 and 100 mA/g.

1:1 ratio exhibits the optimal performance with the highest capacity and Coulombic efficiency (CE) (figs. S5 and S6). This composite has the stoichiometry of $Fe_4(Li_3PO_4)_3(LiF)_3$, referred to as IronPF, and is selected for further studies. IronPF integrates the attributes of both Fe/LiF and Fe/Li_3PO_4 by delivering a high reversible discharge capacity of 285 mAh/g at a current rate of 30 mA/g and an average discharge potential of 2.8 V, corresponding to a specific energy comparable to the NCA and NMC cathodes (Fig. 1C). At 60°C, IronPF exhibits a higher capacity of 368 mAh/g, corresponding to a specific energy of 940 Wh/kg (fig. S7). Regarding the volumetric capacity, the calculated theoretical densities for the pristine and charged states of the active mass are 3.35 and 3.19 g/cm^3, respectively. These values are typical for compounds containing iron.

The cyclic voltammetry (CV) curves further illustrate the enhanced redox behavior of the ternary electrode (Fig. 1D). For the Fe/Li_3PO_4 electrode, an anodic peak is observed at 3.29 V, indicative of the delithiation process transforming Fe/Li_3PO_4 into $FePO_4$. During lithiation, cathodic peaks manifest at 2.98 and 2.08 V, which correspond to the reduction pathways from $FePO_4$ to $LiFePO_4$ and further from $LiFePO_4$ to Fe/Li_3PO_4, respectively. The Fe/LiF electrode displays two anodic peaks at 2.94 and 3.42 V, suggesting the formation of ferrous fluoride and ferric fluoride, in that order. This process is reversed in the cathodic scan, with FeF_3 being sequentially reduced to FeF_2 and then to Fe/LiF, as evidenced by peaks at 2.98 and 1.67 V. In the case of the IronPF electrode, a singular anodic peak at 3.43 V indicates the reversible conversion of Fe/Li_3PO_4/LiF to a solid solution of $FePO_4/FeF_3$. The cathodic scan for IronPF shows a primary peak at 3.04 V, followed by a notably lower cathodic current compared to Fe/LiF. The pronounced specific current of IronPF, when compared to that of Fe/LiF and Fe/Li_3PO_4, corroborates its superior capacity.

The IronPF electrode exhibits stable cycle life at 100 mA/g (Fig. 1E). In addition, IronPF demonstrates superior discharge capacities across all tested current rates. Notably, it retains a capacity of 146 mAh/g even at a high current rate of 1000 mA/g (*41*), in contrast to 118 and 65 mAh/g for Fe/LiF and Fe/Li_3PO_4, respectively, at the same current rate (Fig. 1F). The IronPF electrode also exhibits stable cycle life at both 30 and 100 mA/g at 60°C (Fig. 1G).

One question pertains to the feasibility of fabricating iron-based LSC cathode in an ambient environment, especially given that LSC cathodes in this study were processed and handled in an argon atmosphere. To address this, IronPF electrodes were subjected to dry air for a duration of 2 hours before performance evaluation. The subsequent testing indicated that exposure to air does not detrimentally affect either the capacity or the cycling stability of the IronPF electrodes (fig. S8).

Manganese represents an economical alternative for the LSC cathode material. Pursuing this avenue, we synthesized a MnPF electrode analogous to IronPF by ball milling a stoichiometric blend of manganese metal, Li_3PO_4, and LiF, maintaining a 1:1:1 molar ratio. The initial electrochemical performance demonstrated a relatively low discharge capacity below 150 mAh/g, as indicated by the nearly linear-slope GCD profiles following the first charge, coupled with a modest initial CE of 37.4% (fig. S9). While these preliminary outcomes do not rival the performance of IronPF, the prospect for enhancement in the manganese-based LSC cathode is promising, contingent upon further structural optimization of the electrode.

Operation mechanism of the IronPF cathode

We characterized the pristine, fully charged, and fully discharged iron electrode. As shown by the x-ray diffraction (XRD) patterns (Fig. 2A), ball milling reduces the crystalline salts of LiF and Li_3PO_4 phases to be amorphous. After ball milling, iron remains crystalline but with a much shorter coherence length, i.e., 260 nm, according to the Scherrer equation. XRD patterns reveal that the first charge process transforms the crystalline iron into the amorphous phase of iron salts, and subsequent discharge did not restore the crystallinity of the iron metal phase. We used synchrotron x-ray studies to investigate the valence states of iron during cycling. Soft x-ray absorption (sXAS) results indicate that after the first charge, the primary oxidation state of iron in IronPF lies between Fe(II) and Fe(III); however, no Fe^0 was detected in sXAS after the following discharge (Fig. 2B). On the other hand, hard XAS (hXAS) results suggest that the Fe^0 signal diminished after charging and recovered to some extent after the following discharge (Fig. 2C). The difference between the sXAS and hXAS results is attributed to the vastly different probing depths: While sXAS probes the top surface of the specimen with a depth of ~10 nm, hXAS collects signals throughout the entire sample. The combined findings suggest that iron salts ($FePO_4$ and FeF_3) completely cover the iron metal throughout cycling. The extended x-ray absorption fine structure (EXAFS) results confirm the formation of iron salts: The iron-anion correlation is reversibly strengthened and weakened during the charging and discharge process, respectively (Fig. 2D). We conducted x-ray photoelectron spectroscopy measurements to investigate the surface chemical environment of elements in the electrode at different state of charge (SoC). Figure S10A illustrates that upon charging, there is a notable shift in the P 2p peak to a higher binding energy—greatly surpassing the energy levels observed in pure $FePO_4$ (*42*). This shift suggests that phosphate and fluoride anions are likely coordinated with the same iron ions, with the fluoride's electron-withdrawing inductive effect elevating the binding energy of phosphorus in the PO_4^{3-} group. Notably, upon discharging, the P 2p peak returns to the binding energy characteristic of phosphate in Li_3PO_4, implying reversibility in the chemical environment. In contrast, the F 1s peak demonstrates only a marginal shift, suggesting that the fluoride ions' chemical environment remains largely unaffected by the coordination with either Li^+ or Fe^{3+} ions (fig. S10B).

The scanning transmission electron microscopy (STEM) imaging and the corresponding energy-dispersive x-ray spectroscopy (EDX) mappings reveal a unique composite structure of the pristine IronPF composite. Embedded in the composite particles, iron domains, as shown by the brighter pixels inside STEM images and the EDX elemental mapping, exist as nano-chips, 100 to 200 nm long (Fig. 2E). The anions of fluoride and phosphate are well mixed in this composite, albeit with fluoride enriched around the iron chips. Note that carbon from 20 wt% graphite is uniformly distributed in the composite after ball milling. The better electrochemical properties of IronPF prompt the question of whether a solid solution of phosphate and fluoride is retained after the charging process in the resulting iron salts and after the discharging process in the resulting lithium salt/iron composite. As shown in Fig. 2F, after charging, the "shiny" iron nano-chips vanished, and all EDX signals of iron, phosphorus, and fluorine completely overlapped across the composite particles, thus forming a single complex glassy phase. After the following discharge, the P and F signals remain mixed but with a minor phase separation at a nanoscale, as shown in Fig. 2G. The STEM/

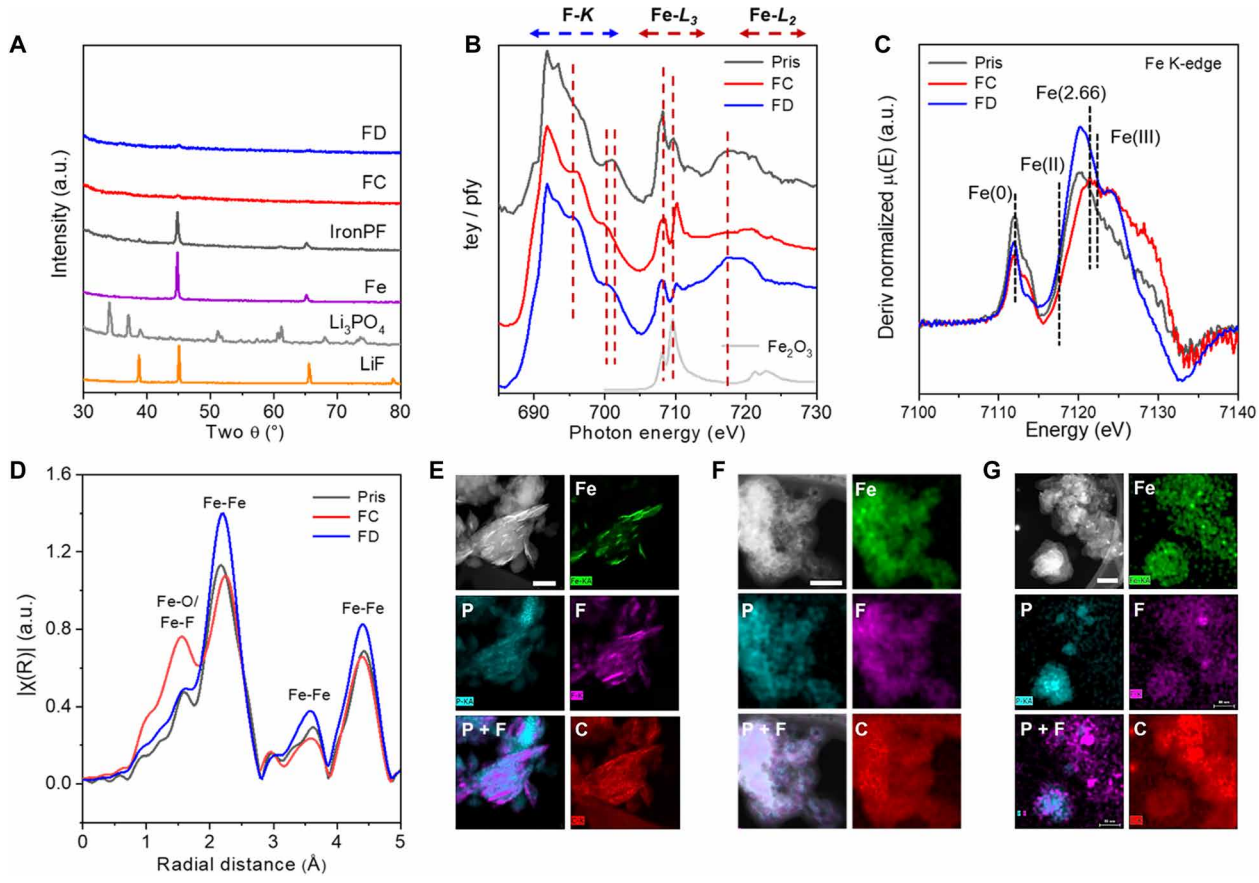

Fig. 2. Operation mechanism of the IronPF cathode. (**A**) Ex situ XRD patterns of the IronPF cathode at the pristine, fully charged (FC), and fully discharged (FD) state during the first charge-discharge cycle of the IronPF || Li cells in comparison with the precursors. (**B** to **D**) Ex situ sXAS spectra, ex situ hXAS, and Fe K-edge EXAFS spectra for the pristine (Pris), fully charged, and fully discharged IronPF cathode during the first cycle. STEM images and the corresponding EDX mappings of the (**E**) pristine (scale bar, 200 nm), (**F**) fully charged (scale bar, 80 nm), and (**G**) fully discharged IronPF cathode (scale bar, 80 nm) during the first cycle.

EDX results demonstrate that throughout the cycling, the anions of phosphate and fluoride constitute a homogeneous anion solid solution after charging and remain well mixed at the discharged state. After discharge, iron signals in the EDX mapping become more locally concentrated, which matches the bright pixels in the STEM imaging and is attributed to the metallic iron nanoparticles, ~10 to 30 nm large. This attests that the discharge process reversibly converts iron salts back to iron metal.

The ex situ TEM results in Fig. 3 (A and B) demonstrate that the disordered phases of Fe, Li_3PO_4, and LiF are discernible through a selected area electron diffraction (SAED) analysis performed on a substantial region of the IronPF. A detailed examination by high-resolution TEM (HRTEM) imaging provides evidence of the short-range order within the LiF and Li_3PO_4 fringes (Fig. 3C), a finding substantiated by the fast Fourier transform pattern (Fig. 3D). Upon charging, the electrode's SAED pattern is characterized by the presence of weak iron lattice rings alone, aligning with XRD data and supporting the formation of an amorphous phase of the resultant iron salts, i.e., $FePO_4/FeF_3$ (Fig. 3, E and F). The HRTEM image shows nanosized fringes of the lattices of $FePO_4$ and FeF_3, which are too weak to generate diffractions (Fig. 3G). Subsequent to discharge, SAED and HRTEM indicate not only the reemergence of the LiF and Li_3PO_4 phases but also a persistence of the disorganized iron phase (Fig. 3, H to K). Accordingly, the charging and discharging processes of the IronPF cathode can be described by the following equation

$$4Fe + 3Li_3PO_4 + 3LiF \underset{\text{Discharge}}{\overset{\text{Charge}}{\rightleftarrows}} 3FePO_4 + FeF_3 + 12Li^+ + 12e^- \quad (1)$$

Ion transport in the LSC cathode

The observed charging capacity of all LSC electrodes suggests the proceeding of the thermodynamically demanded transfer of anions and the migration of iron ions during the oxidation of iron (*43*). During charge, Li_xA dissociates, where Li-ions on the surface of the Li_xA domains get solvated by the electrolyte, and a coordinating anion either migrates inward or is charge-compensated by an incoming Li-ions from the inner parts of the domain. Taking LiF as an example, upon solvating a Li-ion, the F^- ion will get incorporated in the formation process of iron fluorides. Since F^- may not be solvated and transported by the electrolyte to the iron/iron fluoride phase, either solid-state transport of F^- takes place or stripped Fe-ions migrate toward the surface of Li_xA domains (schematically depicted in Fig. 4A). For the discharge process, the desolvated Li-ions attack the iron salts to form Li_xA salts and iron metal particles, where this process is more likely to be controlled by Li-ion

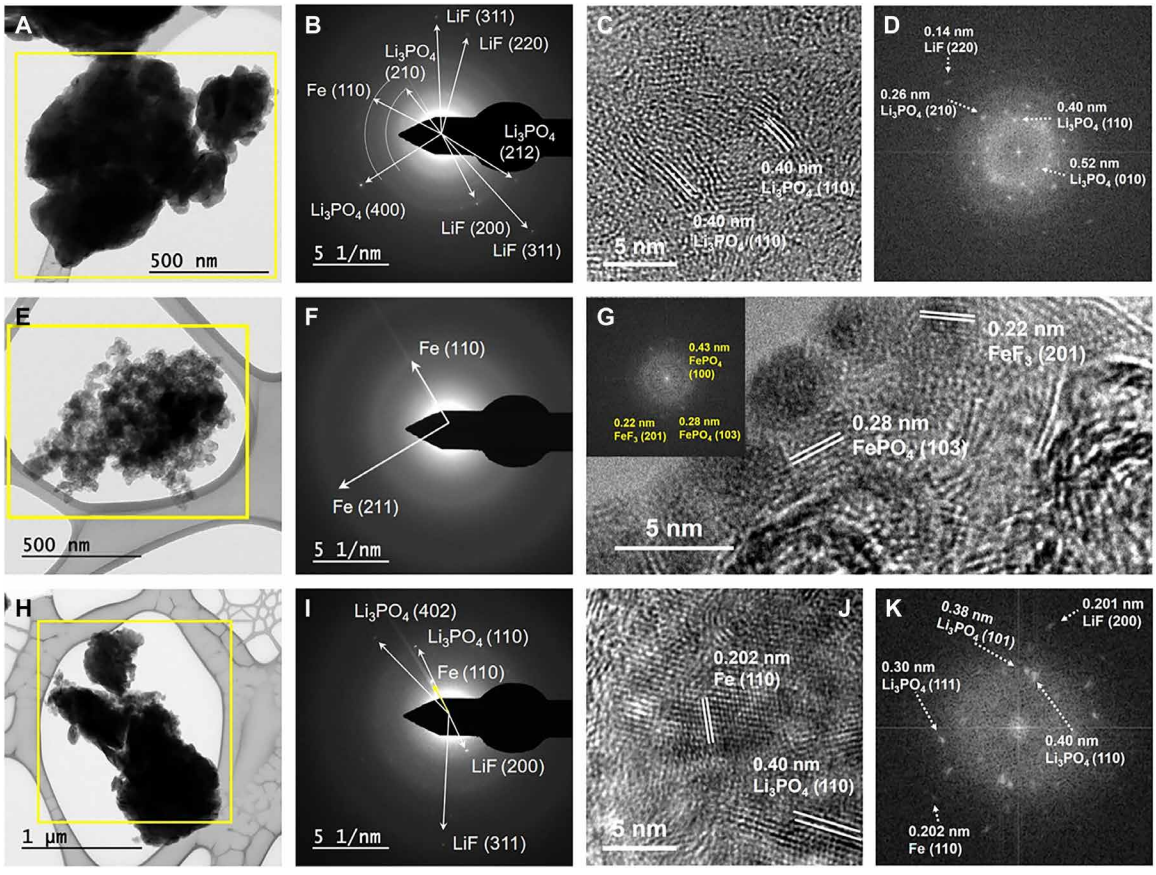

Fig. 3. The phase evolution of the IronPF cathode after charge and discharge in the first cycle. Pristine IronPF: (**A**) TEM image and (**B**) the associated SAED pattern, (**C**) HRTEM image and (**D**) the corresponding fast Fourier transform pattern. Fully charged IronPF: (**E**) TEM image and (**F**) the associated SAED pattern, (**G**) HRTEM image and the corresponding fast Fourier transform pattern (inset). Fully discharged IronPF: (**H**) TEM image and (**I**) the associated SAED pattern, (**J**) HRTEM image and (**K**) the corresponding fast Fourier transform pattern.

conduction through the amorphous Li_xA. Our STEM results (Fig. 4B) show that after charging, the composite electrode exhibits a hollow shell structure, where the holes are about 20 to 30 nm large. The hollow shell structure suggests that Fe-ions are stripped from iron metal during charge, and these Fe-ions are moving outward. On the other hand, the sizes of holes are smaller than the domain size of iron (100 to 200 nm), as shown by Fig. 2E, which indicates that anions have moved to intercept Fe-ions. The anion transport under the electric field across the Li_xA phase and the resulting iron salts obeys the Mott-Cabrera mechanism (*44*). The anion transport can be promoted by the amorphous lithium salt phases that contain ample structural defects and grain boundaries (*45*). It is a question whether phosphate can serve as the charge carrier for the cathode. To address this question, we prepared a ball-milled composite graphite and Li_3PO_4 with a mass ratio of 1:4. Impressively, this LSC cathode exhibits a reversible capacity of 117.5 mAh/g and its GCD profiles differ from the storage of PF_6^- anions from the electrolyte in DIBs (fig. S11) (*46*, *47*). The results suggest the solid diffusion of PO_4^{3-} as the charge carriers for the anodic oxidation of the graphite active mass.

The transport of cations (Li^+ and Fe^{3+}) and anions (F^- and PO_4^{3-}) across tens of nanometers during the charge and discharge of the LSC cathodes is complex and beyond first principles atomistic modeling. Because solid-state Li^+ transport is fast due to its smaller size, we postulate that Fe^{3+} and F^-/PO_4^{3-} diffusions are the bottleneck, which can be facilitated by the anion solid solution. To test this hypothesis for Fe^{3+} diffusion, we have constructed an atomistic model for IronPF (see the Supplementary Materials) and compared the activation energy of Fe^{3+} diffusion from density functional theory among $FePO_4$, FeF_3, and IronPF: As shown in Fig. 4C, Fe^{3+} ions have the lowest activation energy in IronPF, which contributes to efficient Fe utilization and faster kinetics during cycling.

To further unravel the kinetic and transport properties of the LSC cathodes, we conducted galvanostatic electrochemical impedance spectroscopy (GEIS) measurements over half cells. In GEIS, a periodic sinusoidal current formed by overlapping an AC and a DC serves as the perturbation, and the resulting voltage is recorded to generate the impedance spectra (see the Supplementary Materials). The GEIS differs from the conventional EIS data because the testing cell does not flip the direction of the electrode polarization during the measurement. Figure S12 shows the Nyquist plots of GEIS spectra at different SoCs for three composite electrodes. A simple comparison shows that Fe/LiF has a higher impedance than the other two LSC electrodes. To understand more detailed kinetic and transport properties, we carried out an analysis of the distribution of relaxation times (DRT) with the DRT curves fitting the experimental data, where the impedance data are deconvoluted into several

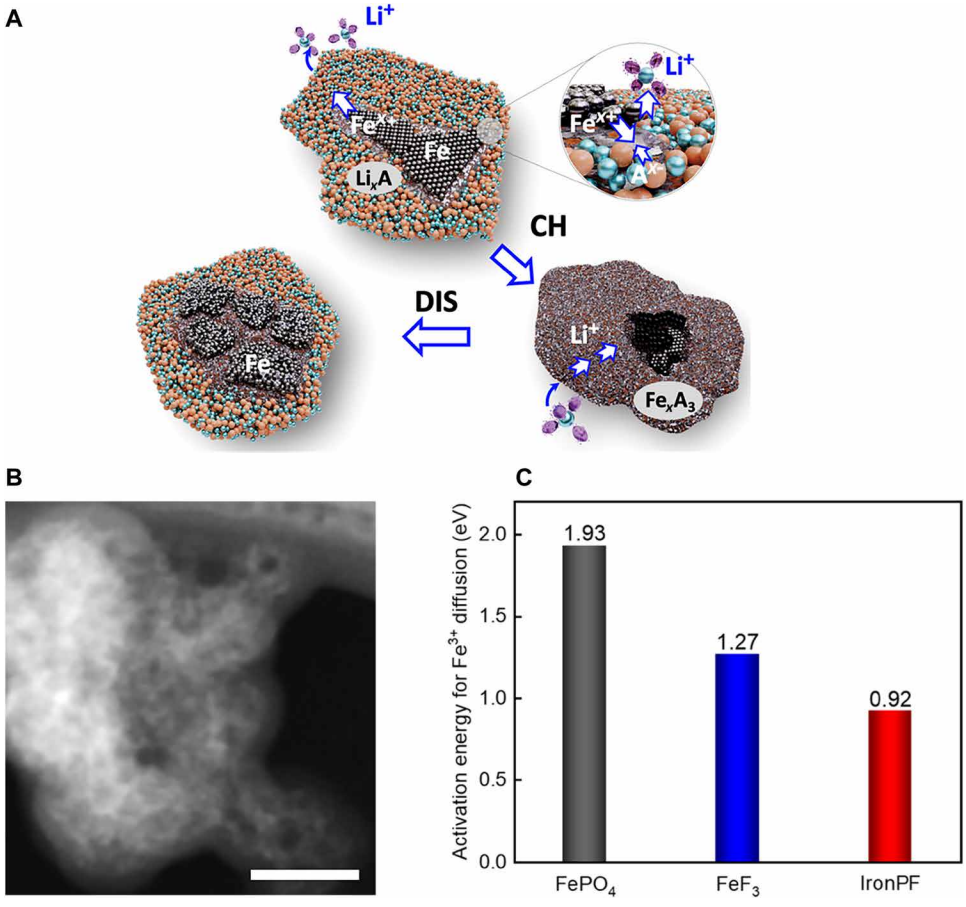

Fig. 4. Ion transport for the LSC cathode. (**A**) Schematic of the operation mechanism of the iron-based LSC cathode. (**B**) STEM image of the fully charged IronPF cathode (scale bar, 80 nm), an enlarged version of the STEM image in Fig. 2F. (**C**) DFT-computed activation energies of Fe^{3+} ion diffusion in iron salts.

Resistor-Constant Phase Element circuits connected in series with increasing time constants.

Figure 5 (A to C) depicts the DRT results of the electrodes as a function of their SoC for a full cycle. The DRT results exhibit four primary components with characteristic time constants, where the component faster than 1×10^{-5} s should be attributed to the electronic contacts, i.e., the equivalent series resistance, R_{ESR}, of the half cells and the R_{ESR} of the IronPF electrode is the lowest. The next component with a time constant between 1×10^{-5} s and 1×10^{-4} s can be attributed to the charge transfer on the iron/iron salt interface, i.e., $R_{CT\text{-}LSC}$, by comparing to the GEIS of the IronPF || IronPF symmetric cells (Fig. 5D). The IronPF electrode exhibits the smallest $R_{CT\text{-}LSC}$, which demonstrates the advantages of ion transport, i.e., Fe-ions and anions, across the interphase of the electrode. By comparing the $R_{CT\text{-}LSC}$ of different LSC cathodes for the discharge process, one can conclude that the solid solution is particularly conducive to Li-ion conduction where the discharge transfer resistance is smaller for IronPF than for Fe/LiF and Fe/Li_3PO_4. In particular, the large discharge $R_{CT\text{-}LSC}$ of Fe/LiF explains the significant potential hysteresis of the Fe/LiF electrode.

The next component with time constants between 1×10^{-4} s and 1×10^{-3} s should be ascribed to the lithium charge transfer resistance, $R_{CT\text{-}Li}$, based on the comparison with the GEIS results of the Li || Li symmetric cell (Fig. 5E). It is worth emphasizing that the charge transfer of the LSC cathode is faster and involves a lower resistance than that of Li metal anode. The fast kinetics of the LSC cathode is likely due to the concerted transport of Fe-ions, anions, and Li-ions. Intriguingly, this time constant is associated with the most conspicuous differences between the three LSC cathode half cells. Again, the IronPF electrode has a smaller $R_{CT\text{-}Li}$ than the other two electrodes during both charge and discharge. IronPF shows a higher $R_{CT\text{-}Li}$ during the charging process than its discharge. The RC time constant, τ, of the $R_{CT\text{-}Li}$ for IronPF, decreases along the SoC of charging, which is initially similar to the longer τ for Fe/LiF and is later shortened to resemble the shorter τ for Fe/Li_3PO_4. The $R_{CT\text{-}Li}$ for the Fe/Li_3PO_4 half cell is consistent. The $R_{CT\text{-}Li}$ of the Fe/LiF half cell is much larger than the other two cells, and it progressively increases along cycling, which pertains to the larger solubility of FeF_3 in the electrolyte. As shown by the UV-Vis spectrum of the electrolyte in contact with FeF_3 (fig. S13), FeF_3 is slightly soluble in the ethylene carbonate/diethyl carbonate (EC/DEC) electrolyte. It is interesting that the solid solution of $FeF_x/Fe_3(PO_4)_x$ is less soluble than FeF_x.

Last, the DRT section with the largest time constant is attributed to the ion diffusion through solid-state phases by comparing the DRT results of half cells and symmetric cells, where again Fe/LiF suffers higher resistance values than IronPF and Fe/Li_3PO_4. The solid solution of IronPF is likely a better conductor for all pertinent ion charge carriers, i.e., Fe-ions, anions, and Li-ions.

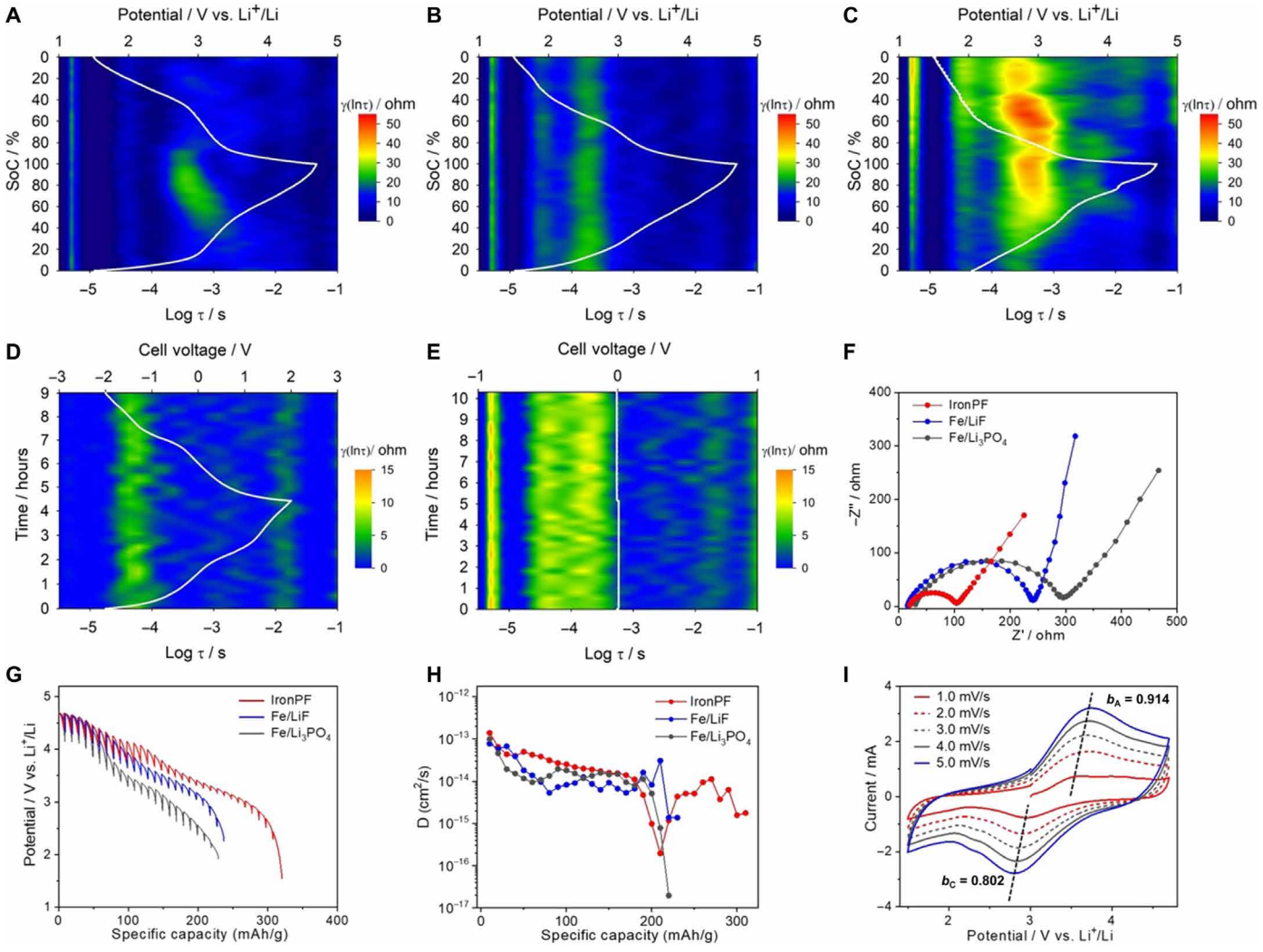

Fig. 5. Studies of kinetics and ion transport for the LSC cathodes. Two-dimensional (2D) DRT contour plots of (**A**) IronPF || Li cell, (**B**) Fe/Li_3PO_4 || Li cell, and (**C**) Fe/LiF || Li cell, derived from the GEIS results. 2D DRT contour plots of (**D**) IronPF || IronPF symmetric cell and (**E**) Li || Li symmetric cell, derived from the GEIS results. (**F**) EIS spectra collected at the anodic peak potential of the Fe/LiF || Li cell, Fe/Li_3PO_4 || Li cell, and IronPF || Li cell. (**G**) GITT measurements of the IronPF || Li cell, Fe/LiF || Li cell, and Fe/Li_3PO_4 || Li cell during charging, and (**H**) corresponding ionic diffusion coefficients, *D*, of the above cells. (**I**) CV curves of the IronPF electrode at the scan rates of 1 to 5 mV s^{-1}.

We also took in situ EIS spectra by using a potential amplitude at the middle potential between the paired anodic and cathodic peaks in CV, where the solid solution of IronPF also exhibits a smaller R_{CT} of 64 ohms than that of Fe/LiF (163 ohms) and Fe/Li_3PO_4 (230 ohms) (Fig. 5F and fig. S14). Despite Fe/LiF having the smallest particle size and both Fe/Li_3PO_4 and IronPF exhibiting relatively larger particle sizes, as depicted in fig. S1 (B to D), IronPF still presents a smaller R_{CT}. This suggests that the diminished R_{CT} is likely due to the faster ion transport. On the basis of the EIS spectra collected at different temperatures, IronPF exhibits the lowest calculated activation energy barrier compared with the other two composite electrodes (fig. S15). The galvanostatic intermittent titration technique (GITT) was used to examine the kinetics of the iron active mass within these salts during charging (Fig. 5G), where the solid solution of IronPF also exhibits a smaller overpotential compared to Fe/LiF and Fe/Li_3PO_4, whereas the diffusion coefficients of ions were estimated to be 10^{-16} to 10^{-13} cm^2 s^{-1} (Fig. 5H).

CV curves collected at different scan rates can reveal the kinetic behaviors of the LSC cathodes (fig. S16). We calculated the *b* values in the equation of $i = av^b$ for IronPF, Fe/LiF, and Fe/Li_3PO_4. When the scan rate is increased from 1 to 5 mV/s, the anodic peak of IronPF and Fe/Li_3PO_4 remains non–diffusion-controlled with *b* values above 0.90, whereas the anodic conversion in Fe/LiF is overwhelmingly diffusion-controlled by having *b* values below 0.6 (Fig. 5I and fig. S16). Fe/Li_3PO_4 exhibits the highest *b* value of the cathodic peak, which is consistent with the finding that Li-ion transport is faster in the amorphous Li_3PO_4 (*48*).

DISCUSSION

Our findings demonstrate that in amorphous solids, anions and Fe-ions play a role beyond being static components for framework construction; instead, they function as mobile charge carriers in the anodic conversion reaction from iron to its corresponding salts.

Lithium salt composite cathodes that comprise an amorphous solid solution of anions transform the reactivity of iron active mass with enhanced utilization, faster reaction kinetics and transport of ions, and stable cycling. The performance of IronPF is among the best for lithium salt composite cathodes (table S1). Our findings open up an approach centered on anion design to breaking the energy density ceiling of LIBs set by nickel-based cathodes with more sustainable Fe-based electrode materials.

MATERIALS AND METHODS

Synthesis of the IronPF composite

To prepare the IronPF composite, we used Li_3PO_4 (TCI AMERICA), LiF (Thermo Fisher Scientific), iron powder (Sigma-Aldrich), and graphite (Sigma-Aldrich) without any prior purification. Li_3PO_4, LiF, and iron powder, in the molar ratio of 3:3:4 (6:3:7 and 3:6:5), were added to a planetary ball mill (Pulverisette 6; Fritsch) along with an additional 20 wt % graphite. The mixture was sealed in an Ar-filled glove box with H_2O and O_2 concentrations below 0.1 part per million (ppm). The mixtures in the bowl were subjected to ball milling at 400 rpm for 50 hours, with a 5-min break every 30 min.

Synthesis of Fe/Li_3PO_4, Fe/LiF, Fe/Li_2CO_3, and Fe/Li_2SO_4 composites

We prepared the composites in the same way as the synthesis of the IronPF composite except for the components and molar ratios. These composites were processed by ball milling (Pulverisette 6; Fritsch) a mixture comprising bulk iron powder, individual lithium salts, and graphite (20 wt %) under an Ar atmosphere with Fe/Li_xA molar ratios corresponding to the three-electron transfer of iron to form ferric Fe_xA_3.

Synthesis of the MnPF composite

We prepared the Mn/Li_3PO_4/LiF composite in the same way as the synthesis of the IronPF composite with a 1:1:1 molar ratio between Mn, Li_3PO_4, and LiF. The composite was processed by ball milling (Pulverisette 6; Fritsch) a mixture comprising bulk Mn powder, lithium salts, and graphite (20 wt %) under an Ar atmosphere.

Synthesis of the Li_3PO_4/graphite composite

We prepared the Li_3PO_4/graphite composite in the same way as the synthesis of the IronPF composite. For the composite, a mixture of Li_3PO_4 and graphite with a mass ratio of 4:1 was processed by ball milling (Pulverisette 6; Fritsch).

Materials characterization

XRD patterns were collected on a Rigaku Ultima IV diffractometer with the Cu Kα radiation (λ = 1.5406 Å). The microstructure and morphology were evaluated by using FEI NOVA 230 field-emission scanning electron microscopy. STEM and its corresponding energy-dispersive EDX were conducted on FEI Titan 80-300 high-resolution STEM with four embedded Bruker SDD detectors. The hXAS and EXAFS measurement of Fe was carried out at the 7-BM QAS beamline at National Synchrotron Light Source II, Brookhaven National Laboratory. The sXAS analysis was performed at BL8.0.1 of Advanced Light Source at Lawrence Berkeley National Laboratory. To prepare the samples, the corresponding cells are disassembled, and the electrodes are washed with dimethyl carbonate and dried in an Ar-filled glove box. The electrodes are sealed using Kapton tape to avoid air exposure.

Electrochemical measurements

The working electrode comprises 80 wt % active materials (IronPF, Fe/Li_3PO_4, Fe/LiF, Fe/Li_2CO_3, Fe/Li_2SO_4, MnPF, or Li_3PO_4/graphite), 10 wt % KetjenBlack carbon, and 10 wt % polyvinylidene fluoride binder. Conductive carbon-coated aluminum foil (MTI Corp.) was used as the current collector. *N*-methyl-2-pyrrlidinone (TCI) solvent was used to make the cathode slurry. The slurry-coated current collectors were dried under a vacuum at 60°C for 12 hours and then punched into discs 12 mm in diameter. Li foil works as the counter and reference electrode. Glass fiber membranes (GF/F, Whatman) were used as the separator. The mass loading of the electrodes is from ~2.1 to 2.5 mg/cm^2, and the specific capacity of the electrodes was calculated on the basis of the mass of Fe and the corresponding lithium salts. $LiPF_6$, 1 M, in EC/DEC (1:1 by volume) was used as the electrolyte. The cells were assembled in an Ar-filled glove box with the concentration of H_2O and O_2 below 0.1 ppm. We tested the electrochemical performance of the cathodes on a Landt CT3002A battery testing system at various current rates. The cutoff potential window was set to 1.5 to 4.7 V versus Li^+/Li. CV and EIS were tested on a VMP-3 multichannel workstation at a scan rate of 0.2 mV/s and a frequency range of 0.01 to 10^5 Hz, respectively.

In GITT experiments, the cycling process involved current pulses of 30 mA/g for 20 min, alternating with 120-min rest to attain quasi-equilibrium potentials. The apparent ionic diffusion coefficients (D) of the composite cathode at different SoC were estimated from the GITT measurements using the following relationship

$$D = \frac{4}{\pi\tau}\left(\frac{R_s}{3}\right)^2\left(\frac{\Delta E_s}{\Delta E_t}\right)^2$$

where τ is the rest time, R_s is the radius of the particles, ΔE_s is the voltage change induced by constant current pulses, and ΔE_t is the voltage change during constant current pulses.

Galvanostatic electrochemical impedance spectroscopy

GEIS was conducted using a VMP-3 electrochemical workstation (BioLogic). Cells were run for 10 cycles at room temperature on a Landt battery cycler (1.5 to 4.7 V, 100 mA/g) before being transferred to a 30°C battery test chamber. After 3 hours of rest, constant current charge-discharge cycles were run at 30 mA/g. During these cycles using DC inputs, EIS measurements were conducted by adding AC signals of 10 mA/g amplitude to the DC signal. To minimize the influence of AC signals on the cycling performance of the cell, 15-min intervals were used between every EIS measurement. The frequency range used was from 200 kHz to 2 Hz, and each measurement took about 27 s to complete. Lower frequencies were not used because continuous increase/decrease of voltage during charge/discharge makes the low-frequency data noisy and unreliable. We conducted a DRT analysis for every EIS data using MATLAB-based DRT tools developed by Wan *et al.* (*49*). Default parameters were used to calculate γ(ln τ) versus τ.

Computational methods

Density functional theory (DFT) calculations were performed by using the Vienna ab initio simulation package [VASP 6.3.2 (*50*)] with projector-augmented waves, pseudopotentials, and the

exchange-correlation functionals parametrized by Perdew, Burke, and Ernzerhof for the generalized gradient approximation (*51*) with a cutoff energy of 500 eV. The onsite Coulomb correction (U-J = 5 eV) (*52*, *53*) is incorporated to accurately depict the localized electronic states of Fe 3d in mixed-valence metals. The convergence criteria for energy and force are set as 10^{-5} eV and 0.02 eV A^{-1}, respectively. A 5 × 5 × 5 Monkhorst-Pack grid is used to sample the electron's Brillouin zone. The minimum-energy pathway and Fe-ion diffusion barriers in Fe salts are determined using the climbing-image nudged elastic band method, as implemented in VASP (*54*, *55*).

The $Fe_4(PO_4)_3F_3$ structure stems from the $Al_4(PO_4)_3(OH)_3$ archetype (*56*). To ensure the integrity of the structures for $Fe_4(PO_4)_3F_3$, we introduce the mixing energy ΔE_{mix} for Fe salts, which is

$$\Delta E_{mix} \ {}^{1}/_{3}E\left[Fe_4(PO_4)_3F_3\right] - {}^{1}/_{3}E(FeF_3) - E(FePO_4)$$

Here, $E[Fe_4(PO_4)_3F_3]$, $E(FeF_3)$, and $E(FePO_4)$ denote the DFT-calculated energies for $Fe_4(PO_4)_3F_3$, FeF_3, and $FePO_4$, respectively.

The calculated mixing energy for $Fe_4(PO_4)_3F_3$ is −0.08 eV, a value less than zero. This implies that the predicted structure for $Fe_4(PO_4)_3F_3$ is plausible. The structure of $Fe_4(PO_4)_3F_3$ is shown in fig. S17.

In terms of structure, bulk Fe adopts a body-centered cubic phase, FeF_3 takes on the $R\bar{3}c$ rhombohedral phase, while FeF_2 is in the $P4_2/mnm$ rutile phase. Furthermore, both $FePO_4$ and $LiFePO_4$ are characterized by the orthorhombic *pbnm* phase. Detailed DFT-optimized unit cell parameters for these materials are summarized in table S2. For our calculations, all Fe salts are considered in the ferromagnetic state, given the negligible energy difference between the ferromagnetic and antiferromagnetic states (*52*).

Supplementary Materials

This PDF file includes:

Figs. S1 to S17
Tables S1 and S2
References

REFERENCES AND NOTES

1. X. Zeng, M. Li, D. Abd El-Hady, W. Alshitari, A. S. Al-Bogami, J. Lu, K. Amine, Commercialization of lithium battery technologies for electric vehicles. *Adv. Energy Mater.* **9**, 1900161 (2019).
2. S. Madhavi, G. V. Subba Rao, B. V. R. Chowdari, S. F. Y. Li, Effect of aluminium doping on cathodic behaviour of $LiNi_{0.7}Co_{0.3}O_2$. *J. Power Sources* **93**, 156–162 (2001).
3. L. Wang, T. Liu, T. Wu, J. Lu, Strain-retardant coherent perovskite phase stabilized Ni-rich cathode. *Nature* **611**, 61–67 (2022).
4. W. Li, S. Lee, A. Manthiram, High-nickel NMA: A cobalt-free alternative to NMC and NCA cathodes for lithium-ion batteries. *Adv. Mater.* **32**, e2002718 (2020).
5. A. Mayyas, D. Steward, M. Mann, The case for recycling: Overview and challenges in the material supply chain for automotive li-ion batteries. *Sustain. Mater. Technol.* **19**, e00087 (2019).
6. K. Turcheniuk, D. Bondarev, G. G. Amatucci, G. Yushin, Battery materials for low-cost electric transportation. *Mater. Today* **42**, 57–72 (2021).
7. L. Mauler, F. Duffner, W. G. Zeier, J. Leker, Battery cost forecasting: A review of methods and results with an outlook to 2050. *Energ. Environ. Sci.* **14**, 4712–4739 (2021).
8. Y. Bi, J. Tao, Y. Wu, L. Li, Y. Xu, E. Hu, B. Wu, J. Hu, C. Wang, J.-G. Zhang, Y. Qi, J. Xiao, Reversible planar gliding and microcracking in a single-crystalline Ni-rich cathode. *Science* **370**, 1313–1317 (2020).
9. A. Urban, D. H. Seo, G. Ceder, Computational understanding of Li-ion batteries. *NPJ Comput. Mater.* **2**, 16002 (2016).
10. Q. Huang, T. P. Pollard, X. Ren, D. Kim, A. Magasinski, O. Borodin, G. Yushin, Fading mechanisms and voltage hysteresis in FeF2–NiF_2 solid solution cathodes for lithium and lithium-ion batteries. *Small* **15**, e1804670 (2019).
11. J. O. Besenhard, H. P. Fritz, The electrochemistry of black carbons. *Angew. Chem. Int. Ed.* **22**, 950–975 (1983).
12. T. Placke, A. Heckmann, R. Schmuch, P. Meister, K. Beltrop, M. Winter, Perspective on performance, cost, and technical challenges for practical dual-ion batteries. *Joule* **2**, 2528–2550 (2018).
13. J. R. Dahn, J. A. Seel, Energy and capacity projections for practical dual-graphite cells. *J. Electrochem. Soc.* **147**, 899 (2000).
14. M. Yu, Y. Sui, S. K. Sandstrom, C. Y. Wu, H. Yang, W. Stickle, W. Luo, X. Ji, Reversible copper cathode for nonaqueous dual-ion batteries. *Angew. Chem. Int. Ed.* **134**, e202212191 (2022).
15. T. C. Gallagher, C. Y. Wu, M. Lucero, S. K. Sandstrom, L. Hagglund, H. Jiang, W. Stickle, Z. Feng, X. Ji, From copper to basic copper carbonate: A reversible conversion cathode in aqueous anion batteries. *Angew. Chem. Int. Ed.* **134**, e202203837 (2022).
16. M. N. Obrovac, J. R. Dahn, Electrochemically active lithia/metal and lithium sulfide/metal composites. *Electrochem. Solid State Lett.* **5**, A70 (2002).
17. P. Liao, B. L. MacDonald, R. A. Dunlap, J. R. Dahn, Combinatorially prepared $[LiF]_{1-x}Fe_x$ nanocomposites for positive electrode materials in Li-ion batteries. *Chem. Mater.* **20**, 454–461 (2008).
18. X. Yu, J. Sun, K. Tang, H. Li, X. Huang, L. Dupont, J. Maier, Reversible lithium storage in LiF/Ti nanocomposites. *Phys. Chem. Chem. Phys.* **11**, 9497–9503 (2009).
19. F. Badway, N. Pereira, F. Cosandey, G. G. Amatucci, Next generation positive electrode materials enabled by nanocomposites: Metal fluoride. *Mater. Res. Soc. Symp.* **756**, 207–218 (2003).
20. R. Prakash, A. K. Mishra, A. Roth, C. Kübel, T. Scherer, M. Ghafari, H. Hahn, M. Fichtner, A ferrocene-based carbon–iron lithium fluoride nanocomposite as a stable electrode material in lithium batteries. *J. Mater. Chem.* **20**, 1871–1876 (2010).
21. T. Li, Z. X. Chen, X. P. Ai, Y. L. Cao, H. X. Yang, LiF/Fe nanocomposite as a lithium-rich and high capacity conversion cathode material for Li-ion batteries. *J. Power Sources* **217**, 54–58 (2012).
22. R. Ma, Y. Dong, L. Xi, S. Yang, Z. Lu, C. Chung, Fabrication of LiF/Fe/graphene nanocomposites as cathode material for lithium-ion batteries. *ACS Appl. Mater. Interfaces* **5**, 892–897 (2013).
23. Y. F. Zhukovskii, P. Balaya, M. Dolle, E. A. Kotomin, J. Maier, Enhanced lithium storage and chemical diffusion in metal-LiF nanocomposites: Experimental and theoretical results. *Phys. Rev. B* **76**, 235414 (2007).
24. C. Wall, R. Prakash, C. Kübel, H. Hahn, M. Fichtner, Synthesis of [Co/LiF/C] nanocomposite and its application as cathode in lithium-ion batteries. *J. Alloys Compd.* **530**, 121–126 (2012).
25. S.-K. Jung, H. Kim, M. G. Cho, S.-P. Cho, B. Lee, H. Kim, Y.-U. Park, J. Hong, K.-Y. Park, G. Yoon, W. M. Seong, Y. Cho, M. H. Oh, H. Kim, H. Gwon, I. Hwang, T. Hyeon, W.-S. Yoon, K. Kang, Lithium-free transition metal monoxides for positive electrodes in lithium-ion batteries. *Nat. Energy* **2**, 1–9 (2017).
26. X. Fan, Y. Zhu, C. Luo, L. Suo, Y. Lin, T. Gao, K. Xu, C. Wang, Pomegranate-structured conversion-reaction cathode with a built-in Li source for high-energy Li-ion batteries. *ACS Nano* **10**, 5567–5577 (2016).
27. Y. Zhao, K. Wei, H. Wu, S. Ma, J. Li, Y. Cui, Z. Dong, Y. Cui, C. Li, LiF splitting catalyzed by dual metal nanodomains for an efficient fluoride conversion cathode. *ACS Nano* **13**, 2490–2500 (2019).
28. J. Jamnik, J. Maier, Nanocrystallinity effects in lithium battery materials part IV. *Phys. Chem. Chem. Phys.* **5**, 5215–5220 (2003).
29. T. Wu, Y. Cui, K. Wei, C. Lai, Y. Zhao, S. Ni, Y. Chen, X. Gao, Y. Cui, C. Li, Catalysis of nickel nanodomains on Li-F dissociation for high-capacity fluoride cathodes with prior delithiation ability. *Nano Energy* **103**, 107843 (2022).
30. X. Hua, A. S. Eggeman, E. Castillo-Martínez, R. Robert, H. S. Geddes, Z. Lu, C. J. Pickard, W. Meng, K. M. Wiaderek, N. Pereira, G. G. Amatucci, P. A. Midgley, K. W. Chapman, U. Steiner, A. L. Goodwin, C. P. Grey, Revisiting metal fluorides as lithium-ion battery cathodes. *Nat. Mater.* **20**, 841–850 (2021).
31. S.-W. Kim, N. Pereira, N. A. Chernova, F. Omenya, P. Gao, M. S. Whittingham, G. G. Amatucci, D. Su, F. Wang, Structure stabilization by mixed anions in oxyfluoride cathodes for high-energy lithium batteries. *ACS Nano* **9**, 10076–10084 (2015).
32. J. Huang, B. Ouyang, Y. Zhang, L. Yin, D. H. Kwon, Z. Cai, Z. Lun, G. Zeng, M. Balasubramanian, G. Ceder, Inhibiting collective cation migration in Li-rich cathode materials as a strategy to mitigate voltage hysteresis. *Nat. Mater.* **22**, 353–361 (2023).
33. Z. Lun, B. Ouyang, D.-H. Kwon, Y. Ha, E. E. Foley, T.-Y. Huang, Z. Cai, H. Kim, M. Balasubramanian, Y. Sun, J. Huang, Y. Tian, H. Kim, B. D. McCloskey, W. Yang, R. J. Clément, H. Ji, G. Ceder, Cation-disordered rocksalt-type high-entropy cathodes for Li-ion batteries. *Nat. Mater.* **20**, 214–221 (2021).
34. F. Badway, N. Pereira, Carbon-metal fluoride nanocomposites. *J. Electrochem. Soc.* **150**, A1209 (2003).
35. C. Yang, J. Chen, X. Ji, T. P. Pollard, X. Lü, C.-J. Sun, S. Hou, Q. Liu, C. Liu, T. Qing, Y. Wang, O. Borodin, Y. Ren, K. Xu, C. Wang, Aqueous Li-ion battery enabled by halogen conversion–intercalation chemistry in graphite. *Nature* **569**, 245–250 (2019).

36. W. Zhao, M. Fang, F. Wu, H. Wu, L. Wang, G. Chen, Preparation of graphene by exfoliation of graphite using wet ball milling. *J. Mater. Chem.* **20**, 5817–5819 (2010).
37. C. Teng, D. Xie, J. Wang, Z. Yang, G. Ren, Y. Zhu, Ultrahigh conductive graphene paper based on ball-milling exfoliated graphene. *Adv. Funct. Mater.* **27**, 1700240 (2017).
38. R. Prakash, C. Wall, A. K. Mishra, C. Kübel, M. Ghafari, H. Hahn, M. Fichtner, Modified synthesis of [Fe/LiF/C] nanocomposite, and its application as conversion cathode material in lithium batteries. *J. Power Sources* **196**, 5936–5944 (2011).
39. Z. Xiong, G. Zhang, L. Mo, M. Zhong, Electrochemical performance of $LiVPO_4F$ synthesized by ball-milling assisted sol-gel method. *Russ. J. Electrochem.* **50**, 1003–1007 (2014).
40. R. Tripathi, T. N. Ramesh, B. L. Ellis, L. F. Nazar, Scalable synthesis of tavorite $LiFeSO_4F$ and $NaFeSO_4F$ cathode materials. *Angew. Chem. Int. Ed.* **49**, 8738–8742 (2010).
41. F. Badway, F. Cosandey, N. Pereira, G. G. Amatucci, Carbon metal fluoride nanocomposites. *J. Electrochem. Soc.* **150**, A1318 (2003).
42. C. Oikonomou, E. Hryha, L. Nyborg, An XPS investigation on the thermal stability of the insulating surface layer of soft magnetic composite powder. *Surf. Interface Anal.* **48**, 445–450 (2016).
43. J. Maier, Pushing nanoionics to the limits: Charge carrier chemistry in extremely small systems. *Chem. Mater.* **26**, 348–360 (2014).
44. S. Qiu, H. F. Lai, J. A. Yarmoff, Self-limiting growth of metal fluoride thin films by oxidation reactions employing molecular precursors. *Phys. Rev. Lett.* **85**, 1492–1495 (2000).
45. T. C. Kaspar, S. D. Taylor, K. H. Yano, T. G. Lach, Y. Zhou, Z. Zhu, A. A. Kohnert, E. K. Still, P. Hosemann, S. R. Spurgeon, D. K. Schreiber, Bulk and short-circuit anion diffusion in epitaxial Fe_2O_3 films quantified using buried isotopic tracer layers. *Adv. Mater. Interfaces* **8**, 2001768 (2021).
46. O. Fromm, P. Meister, X. Qi, S. Rothermel, J. Huesker, H. W. Meyer, M. Winter, T. Placke, Study of the electrochemical intercalation of different anions from non-aqueous electrolytes into a graphite-based cathode. *ECS Trans.* **58**, 55–65 (2014).
47. J. A. Seel, J. R. Dahn, Electrochemical intercalation of PF_6 into graphite. *J. Electrochem. Soc.* **147**, 892 (2000).
48. T. Ohnishi, K. Takada, Sputter-deposited amorphous Li_3PO_4 solid electrolyte films. *ACS Omega* **7**, 21199–21206 (2022).
49. T. H. Wan, M. Saccoccio, C. Chen, F. Ciucci, Influence of the discretization methods on the distribution of relaxation times deconvolution: Implementing radial basis functions with DRTtools. *Electrochim. Acta* **184**, 483–499 (2015).
50. G. Kresse, J. Furthmüller, Efficient iterative schemes forab initiototal-energy calculations using a plane-wave basis set. *Phys. Rev. B* **54**, 11169–11186 (1996).
51. J. P. Perdew, K. Burke, M. Ernzerhof, Generalized gradient approximation made simple. *Phys. Rev. Lett.* **77**, 3865–3868 (1996).
52. M. Mori, S. Tanaka, H. Senoh, K. Matsui, T. Okumura, H. Sakaebe, H. Kiuchi, E. Matsubara, First-principles calculations of the atomic structure and electronic states of Li_xFeF_3. *Phys. Rev. B* **100**, 035128 (2019).
53. R. F. Li, S. Q. Wu, Y. Yang, Z. Z. Zhu, Structural and electronic properties of Li-Ion battery cathode material FeF_3. *J. Phys. Chem. C* **114**, 16813–16817 (2010).
54. G. Mills, H. Jónsson, Quantum and thermal effects in H_2 dissociative adsorption: Evaluation of free energy barriers in multidimensional quantum systems. *Phys. Rev. Lett.* **72**, 1124–1127 (1994).
55. G. Henkelman, B. P. Uberuaga, H. Jónsson, A climbing image nudged elastic band method for finding saddle points and minimum energy paths. *J. Chem. Phys.* **113**, 9901–9904 (2000).
56. P. B. Moore, T. Araki, Trolleite, $Al_4(OH)_3[PO4]_3$: A very dense structure with octahedral face-sharing dimers. *Am. Mineral.* **59**, 974–984 (1974).
57. J. Heo, S.-K. Jung, I. Hwang, S.-P. Cho, D. Eum, H. Park, J.-H. Song, S. Yu, K. Oh, G. Kwon, T. Hwang, K.-H. Ko, K. Kang, Amorphous iron fluorosulfate as a high-capacity cathode utilizing combined intercalation and conversion reactions with unexpectedly high reversibility. *Nat. Energy* **8**, 30–39 (2023).

Acknowledgments: We thank P. Eschbach and J. Razink for work on TEM measurements. Our thanks also extend to Q. Williams of Howard University and C. Chang of Oregon State University for insightful discussions. **Funding:** This work was supported by the US Department of Energy (DOE), Basic Energy Science, award no. DE-SC0023408 (X.J., D.J., and C.W.); the Advanced Light Source, which is a DOE Office of Science User Facility under contract no. DE-AC02-05CH11231; the US DOE, Office of Energy Efficiency and Renewable Energy, Vehicle Technologies Office; the Argonne National Laboratory operated for DOE Office of Science by UChicago Argonne LLC, under contract no. DE-AC02-06CH11357; and the use of the National Synchrotron Light Source II (7-BM, 18 ID, and 28 ID) supported by the US DOE, an Office of Science user facility operated by Brookhaven National Laboratory under contract no. DE-SC0012704. **Author contributions:** Writing—original draft: X.J., M.Y., J.W., and T.L. Conceptualization: X.J., M.Y., D.J., J.W., M.L., and C.W. Investigation: M.Y., X.J., J.W., M.L., M.S.J., Z.Z., S.S., Y.Y., X.Z., W.Y., and T.L. Writing—review and editing: X.J., M.Y., J.W., M.L., M.S.J., Z.Z., W.Y., D.J., and T.L. Methodology: M.Y., M.L., W.Y., D.J., T.L., and X.J. Resources: M.Y., J.W., M.L., C.W., D.J., and X.J. Funding acquisition: X.J., D.J., and W.Y. Data curation: M.Y., J.W., M.L., W.Y., and X.J. Validation: M.Y., J.W., M.L., W.Y., T.L., Y.Y., and X.J. Formal analysis: M.Y., J.W., M.L., and S.S. Supervision: X.J., W.Y., and C.W. Project administration: X.J., M.Y., W.Y., and T.L. Visualization: M.Y., J.W., M.L., M.S.J., S.S., W.Y., D.J., T.L., and X.J. **Competing interests:** X.J. and M.Y. are inventors of a pending US patent application no. 18/510,483, filed by Oregon State University on 15 November 2023. The authors declare no other competing interests. **Data and materials availability:** All data needed to evaluate the conclusions in the paper are present in the paper and/or the Supplementary Materials.

Submitted 10 December 2023
Accepted 16 April 2024
Published 23 May 2024
10.1126/sciadv.adn4441